Available online at www.sciencedirect.com
SCIENCE DIRECT®
Journal of Computational Physics 200 (2004) 695–717
JOURNAL OF COMPUTATIONAL PHYSICS
www.elsevier.com/locate/jcp

A free-surface hydrodynamic model for density-stratified flow in the weakly to strongly non-hydrostatic regime

Colin Y. Shen *, Thomas E. Evans

Naval Research Laboratory, Code 7230, 4555 Overlook Ave. S.W., Washington, DC 20375, USA

Received 13 January 2004; received in revised form 28 April 2004; accepted 29 April 2004
Available online 10 June 2004

Abstract

A non-hydrostatic density-stratified hydrodynamic model with a free surface has been developed from the vorticity equations rather than the usual momentum equations. This approach has enabled the model to be obtained in two different forms, weakly non-hydrostatic and fully non-hydrostatic, with the computationally efficient weakly non-hydrostatic form applicable to motions having horizontal scales greater than the local water depth. The hydrodynamic model in both its weakly and fully non-hydrostatic forms is validated numerically using exact nonlinear non-hydrostatic solutions given by the Dubriel–Jacotin–Long equation for periodic internal gravity waves, internal solitary waves, and flow over a ridge. The numerical code is developed based on a semi-Lagrangian scheme and higher order finite-difference spatial differentiation and interpolation. To demonstrate the applicability of the model to coastal ocean situations, the problem of tidal generation of internal solitary waves at a shelf-break is considered. Simulations carried out with the model obtain the evolution of solitary wave generation and propagation consistent with past results. Moreover, the weakly non-hydrostatic simulation is shown to compare favorably with the fully non-hydrostatic simulation. The capability of the present model to simulate efficiently relatively large scale non-hydrostatic motions suggests that the weakly non-hydrostatic form of the model may be suitable for application in a large-area domain while the computationally intensive fully non-hydrostatic form of the model may be used in an embedded sub-domain where higher resolution is needed.
Published by Elsevier Inc.

1. Introduction

The numerical solution of three-dimensional incompressible hydrodynamic equations invariably involves solving a three-dimensional (3D) elliptic equation, which is usually the most time consuming part of the calculation [1–6]. However, this computational burden can be alleviated significantly if the motion is weakly non-hydrostatic, defined herein as the horizontal scale of the motion exceeding the local water

* Corresponding author.
E-mail address: shen@nrl.navy.mil (C.Y. Shen).

0021-9991/$ - see front matter. Published by Elsevier Inc.
doi:10.1016/j.jcp.2004.04.015

depth. Then it is possible to reduce the dimension of the elliptic equation by one. This computational advantage has been widely adopted in the study of long irrotational surface gravity waves, and the weakly non-hydrostatic equations used for such computation have been referred to as the (extended) Boussinesq equations [7–10]. For rotational density-stratified motion, such as internal gravity waves and shear flows, it has been shown [11] that the reduction of the elliptic equation's dimension by one is equally possible when the rotational motion is weakly non-hydrostatic. The derivation of the more general weakly non-hydrostatic equations, however, requires the free surface hydrodynamic model to be formulated differently, by obtaining a 3D elliptic equation in terms of the vertical velocity from the vorticity equations instead of the usual pressure from the momentum equations. This alternative formulation together with the weakly non-hydrostatic approximation then leads to an elliptic equation of reduced dimension.

For coastal oceanography, it can be advantageous to develop a weakly non-hydrostatic, density-stratified model, as the relatively shallow water depths on the continental shelf render wave/current motions (rotational or not) in many situations weakly non-hydrostatic. Such a model can be utilized to significantly speed up the computation of coastal waves and currents relative to a fully non-hydrostatic model. In this paper, we will present the numerical free-surface hydrodynamic model developed based on the formulation of the elliptic equation in terms of the vertical velocity given in [11]. The model will be presented in both its weakly and fully non-hydrostatic forms. To validate these two forms of the model, the simulated flow fields will be shown and compared to the exact nonlinear non-hydrostatic solutions of the Dubriel–Jacotin–Long (DJL) equation [12], which is also often referred to as Long's equation. The DJL solutions to be compared to are periodic internal waves, internal solitary waves, and flow over a ridge. Following the validation, the model will be applied to a coastal internal wave problem, namely, the tidal generation of internal waves at the shelf-break, to demonstrate the applicability of the weakly non-hydrostatic approximation in the coastal environment.

The paper is organized as follows. In Section 2, the governing equations and the weakly non-hydrostatic approximation are summarized. In Section 3, the numerical solution procedure using a semi-Lagrangian scheme is developed. In Section 4, the solutions of the DJL equation are presented for three cases: periodic internal gravity waves, internal solitary waves, and stratified flow over a ridge. The weakly and fully non-hydrostatic simulations of the wave/current motion in each case are presented and compared to the benchmark DJL solutions. In Section 5, the weakly non-hydrostatic approximation is applied to the simulation of internal wave generation by tides at the shelf-break. In Section 6, the summary is given.

2. Governing equations

In this section, we recapitulate the fully and weakly non-hydrostatic equations derived in [11]. The starting point for that derivation has been the horizontal vorticity equations and the free-surface momentum equation. The horizontal vorticity equations make the non-hydrostatic vertical motion directly accessible to approximations; specifically, setting the part of the horizontal vorticity components related to the vertical motion to zero yields the hydrostatic limit, while the weakly non-hydrostatic approximation is obtained by allowing the same vorticity component to assume a small non-vanishing value. The emphasis on the vertical motion with the horizontal vorticity formulation here may be contrasted with the vertical vorticity formulation, widely used in oceanographic as well as meteorological studies, that emphasizes horizontal currents.

2.1. The fully non-hydrostatic equations

Defining $\mathbf{u}_* = (u, v, w)$ as the velocity vector in the Cartesian coordinate system $\mathbf{x}_* = (x, y, z)$ with z positive upward, the three-dimensional vorticity vector is

$$\mathbf{s}_* = \nabla_* \times \mathbf{u}_* = (s_x, s_y, s_z) = \left(\frac{\partial w}{\partial y} - \frac{\partial v}{\partial z}, \frac{\partial u}{\partial z} - \frac{\partial w}{\partial x}, \frac{\partial v}{\partial x} - \frac{\partial u}{\partial y} \right), \tag{1}$$

where $\nabla_* = (\partial/\partial x, \partial/\partial y, \partial/\partial z)$. Denoting the horizontal vector component of vorticity by $\mathbf{s} = (s_x, s_y)$ and the horizontal vector component of velocity by $\mathbf{u} = (u, v)$, the governing equation for the horizontal vorticity vector is obtained by taking the curl of the momentum equation,

$$\frac{\mathrm{D}\mathbf{u}_*}{\mathrm{D}t} + \mathbf{f} \times \mathbf{u}_* = -\frac{\nabla_* P}{\rho_0} + \mathbf{g}\frac{\rho}{\rho_0}, \tag{2}$$

and is

$$\frac{\mathrm{D}\mathbf{s}}{\mathrm{D}t} = (s_* + \mathbf{f}) \cdot \nabla_* \mathbf{u} - \mathbf{g} \times \frac{\nabla \rho}{\rho_0}, \tag{3}$$

applicable to an incompressible rotating fluid with the Boussinesq approximation for density variation, where $\mathrm{D}/\mathrm{D}t = \partial/\partial t + \mathbf{u}_* \cdot \nabla_*$, ρ is the total density, ρ_0 is a constant reference density, $\mathbf{f} = (0, 0, f)$ is the rotational vector for the Coriolis frequency, $\mathbf{g} = (0, 0, -g)$ is the gravity, and P is the pressure. (Temporarily the viscous terms are omitted for clarity.) The density variation is governed by

$$\frac{\mathrm{D}\rho}{\mathrm{D}t} = 0. \tag{4}$$

It is convenient to define $\mathbf{s}' = (s_y, -s_x)$ in terms of the $\mathbf{s}$ components in (3), and the following vector identity is written

$$\frac{\partial \mathbf{u}}{\partial z} - \nabla w = \mathbf{s}', \tag{5}$$

where $\nabla = (\partial/\partial x, \partial/\partial y)$ is the horizontal gradient operator. $\mathbf{u}$ may be eliminated from (5) by applying the horizontal gradient operator to (5) and making use of the continuity equation

$$\nabla \cdot \mathbf{u} + \frac{\partial \mathbf{w}}{\partial \mathbf{z}} = 0, \tag{6}$$

to obtain an elliptic equation for w,

$$\nabla^2 w + \frac{\partial^2 w}{\partial z^2} = -\nabla \cdot \mathbf{s}'. \tag{7}$$

This equation can be solved for the vertical velocity w given appropriate boundary conditions (discussed further in Section 3.5). Once w is determined, (6) can be integrated downward for $\mathbf{u}$ given a surface horizontal velocity as the boundary condition. Let $\mathbf{u}_\eta$ denote this horizontal velocity at the free surface. The equation governing $\mathbf{u}_\eta$, in the absence of horizontal atmospheric pressure variation, is

$$\left[\frac{\mathrm{D}\mathbf{u}}{\mathrm{D}t}\right]_\eta + \mathbf{f} \times \mathbf{u}_\eta = -\left(\left[\frac{\mathrm{D}w}{\mathrm{D}t}\right]_\eta + g\frac{\rho_\eta}{\rho_0} \right) \nabla \eta, \tag{8}$$

which is (2) evaluated at the free surface with the horizontal pressure gradient at the constant- pressure free surface evaluated in terms of the horizontal gradient of the free surface height, η. The subscript η denotes flow variables evaluated at the free surface.

The free surface height varies according to

$$\frac{\partial \eta}{\partial t} = -\nabla \cdot \int_{-h}^{\eta} \mathbf{u}\, \mathrm{d}z, \tag{9}$$

which is the vertically integrated form of the continuity equation (6), with the application of the boundary conditions at the free surface, $z = \eta$,

$$w_\eta = \frac{\partial \eta}{\partial t} + \mathbf{u}_\eta \cdot \nabla \eta \tag{10}$$

and at the rigid bottom, $z = -h$,

$$w_{-h} = -\mathbf{u}_{-h} \cdot \nabla h. \tag{11}$$

Eqs. (3)–(9) form a set of non-hydrostatic equations governing wave/current motions in a free-surface, density-stratified, hydrodynamic system. By using the vorticity equations as the primary governing equations, the elliptic equation (7) for w appears and must be inverted at each time step of the numerical integration. This contrasts with the conventional approach of integrating the momentum equation (2) directly and inverting at each time step an elliptic equation for P. Although the present approach is different, it does little to change the computational demand, since an elliptic equation still has to be inverted. The main advantage of the horizontal vorticity formulation is that the non-hydrostatic vertical acceleration implicit in the horizontal vorticity component (5) is accessible to approximation. For example, the widely used hydrostatic model equations are readily obtained by setting ∇w in (5) to zero; in which case, the solution of the elliptic equation (7) is unnecessary, and (3) is the governing vorticity equation with $\mathbf{s} = (-\partial v/\partial z, \partial u/\partial z)$, while the free surface momentum equation is (8) with the term $\mathrm{D}w/\mathrm{D}t = 0$. When the non-hydrostatic motion is non-zero but small, i.e., small non-negligible ∇w, the weakly non-hydrostatic approximation can be applied to the w terms in (5) and (7) to obtain an elliptic equation of one less dimension, which can be more efficiently solved than the full 3D elliptic equation (7). This is discussed next.

2.2. The weakly non-hydrostatic equations in the x–z dimension

The degree of the non-hydrostatic influence is typically measured on the basis of the ratio $\mu = h/L$, where L represents a horizontal scale of the wave/current motion and h is the local water depth. With this scaling of x and z, it can be shown that the horizontal derivative terms in (5) and (7) are smaller than the vertical derivative terms by μ^2 for motions having $L > h$. The smallness of this dimensionless parameter suggests that in the case of $\mu^2 \ll 1$, velocity variables can be expanded as a power series of μ^2, and the equations of different orders of accuracy in μ^2 can be obtained. The zeroth order equations are the hydrostatic equations. At the next order the weakly non-hydrostatic equations of μ^2 accuracy are obtained, and still higher-order accuracy equations can be obtained by retaining higher order μ^2 terms. The procedure by which the weakly non-hydrostatic equations are derived has been detailed in [11]. A key step in the derivation is the choice of an intermediate horizontal velocity variable $\tilde{\mathbf{u}}$ to represent, in a vertically averaged sense, the horizontal velocity distribution over the water column. In the subsequent perturbation analysis, a 2D horizontal elliptic equation is derived for this $\tilde{\mathbf{u}}$, and 3D flow is obtained by relating $\tilde{\mathbf{u}}$, the solution of the 2D elliptic equation to the actual velocity vector $\mathbf{u}$. This is a more efficient approach to modeling the weakly non-hydrostatic motion, without real loss of accuracy, than solving the full 3D elliptic equation (7) exactly. In the following we list the two-dimensional (x, z) version of the weakly non-hydrostatic equations of μ^2 accuracy given in [11], for which we will develop the numerical solution procedure, directly extendable to three dimensions.

With the focus here specifically on internal wave/current motions not the surface gravity waves, the vertical acceleration term, $\mathrm{D}w/\mathrm{D}t$, in (8) may be neglected relative to $\mathbf{g}$. The two-dimensional total time

derivative is now $D/Dt = \partial/\partial t + u\partial/\partial x + w\partial/\partial z$. Let $F(\mathbf{u}_\eta)$ denote dissipation, yet to be specified. The governing equation for the surface velocity (8) becomes

$$\left[\frac{D\mathbf{u}}{Dt}\right]_\eta + \mathbf{f}\times\mathbf{u}_\eta = -g\frac{\rho_\eta}{\rho_0}\frac{\partial\eta}{\partial x} + F(\mathbf{u}_\eta). \tag{12}$$

It should be noted that internal wave/current motions will always generate some surface Dw/Dt. In all calculations to be presented, the neglected surface Dw/Dt is much less than $\mathbf{g}$. The surface Dw/Dt clearly cannot be neglected in the dynamics of finite-amplitude surface gravity waves, and the use of (8) in its entirety for surface gravity wave calculation is the same as that already published in the literature as noted in [11].

The evolution equation for surface height equation is now

$$\frac{\partial\eta}{\partial t} = -\frac{\partial}{\partial x}\int_{-h}^{\eta} u\,dz \tag{13}$$

and the time-dependent horizontal vorticity equation is

$$\frac{D\mathbf{s}}{Dt} = s_x\frac{\partial\mathbf{u}}{\partial x} + (s_z+f)\frac{\partial\mathbf{u}}{\partial z} - \mathbf{g}\times\frac{\nabla\rho}{\rho_0} + F(\mathbf{s}), \tag{14}$$

where $s_x = -\partial v/\partial z$, $s_z = \partial v/\partial x$ and $F(\mathbf{s})$ denotes the dissipation.

Defining an intermediate velocity variable, $\tilde{\mathbf{u}}$, representative of the $\mathbf{u}$ distribution over local water depth, the perturbation analysis of (5) and (7) in terms of small parameter $\mu^2(\ll 1)$ carried out in [11] shows that a 2D horizontal elliptic equation for $\tilde{\mathbf{u}}$ accurate to μ^2 can be obtained. In the present one horizontal dimension, applicable to the x-component of $\tilde{\mathbf{u}}$, the equation is of the following form for a stress-free free surface:

$$\left(\frac{H_\eta^2}{3}\right)\frac{\partial^2\tilde{u}}{\partial x^2} + \left(H_\eta\frac{\partial h}{\partial x}\right)\frac{\partial\tilde{u}}{\partial x} + \left(\frac{H_\eta}{2}\frac{\partial^2 h}{\partial x^2} - 1\right)\tilde{u} = -\left(u_\eta + \bar{s}_w\right) + \frac{H_\eta}{2}\left[\left(\frac{\partial h}{\partial x}\right)\frac{\partial}{\partial x}\Delta u_{-h} + \left(\frac{\partial^2 h}{\partial x^2}\right)\Delta u_{-h}\right], \tag{15}$$

where $H_\eta = h+\eta$, $\Delta u(z) = \int_z^\eta s_y\,dz'$, $\Delta u_{-h} = \Delta u(z=-h)$ and

$$\bar{s}_w = \frac{1}{H_\eta}\int_{-h}^{\eta} s_w\,dz \quad \text{with } s_w = -\int_z^\eta \frac{\partial}{\partial x}\left(\int_{-h}^{z}\int_z^\eta \frac{\partial s_y}{\partial x}\,dz'\,dz''\right)dz'''.$$

Once $\tilde{u}$ is determined from (15), the actual horizontal velocity, u, as a function of depth is obtained from the following equation derived in [11]:

$$u(z) = u_\eta - \Delta u(z) + s_w + \frac{1}{2}(H_\eta^2 - H_z^2)\frac{\partial^2\tilde{u}}{\partial x^2} + (H_\eta - H_z)\left[\left(2\frac{\partial h}{\partial x}\right)\frac{\partial\tilde{u}}{\partial x} + \left(\frac{\partial^2 h}{\partial x^2}\right)\tilde{u} - \left(\frac{\partial h}{\partial x}\right)\frac{\partial}{\partial x}\Delta u_{-h} - \left(\frac{\partial^2 h}{\partial x^2}\right)\Delta u_{-h}\right], \tag{16}$$

where $H_z = h+z$.

The vertical velocity is obtained from the continuity equation (6) by integration

$$w(z) = w_{-h} - \int_{-h}^{z}\frac{\partial u}{\partial x}\,dz, \tag{17}$$

where $w_{-h} = -u_{-h}(\partial h/\partial x)$, and $u_{-h} = u(z=-h)$.

Eqs. (15)–(17) are the equations for the weakly non-hydrostatic model in place of (5) and (7).

3. Numerical solution method

There are a number of ways to solve the equations in Section 2 numerically. For the free surface problem, the constantly changing geometry of the fluid domain due to the moving free surface suggests that a finite-difference scheme based on tracking moving fluid-particles may be desirable. The semi-Lagrangian scheme is one such scheme and is used here. This technique for integration of the equations of motion has been discussed extensively [13,14]. The basic idea of the semi-Lagrangian scheme is to calculate the evolving flow field with respect to moving fluid particles but to use a new set of particles at each time step; this procedure requires a spatial interpolation at each time step to re-grid the flow field for the new particles. The procedure described in the following, known also as the forward trajectory calculation, re-grids the flow field after each Lagrangian time step. This has been shown in [14] to lend more stability and efficiency to the semi-Lagrangian scheme than the backward trajectory calculation, i.e., re-griding before the Lagrangian time step.

3.1. The grid system

The positions of the new particles at each time step are defined by a surface conforming grid

$$\xi_j = 1 - 2\frac{\eta - z_j}{\eta + h}, \tag{18}$$

so that ξ_j has the fixed range $-1 \leqslant \xi_j \leqslant 1$ for $-h \leqslant z_j \leqslant \eta$, where the subscript j is the integer index identifying the discrete gird points along the vertical axis. The starting vertical position of a particle thus varies with η from one time step to the next and is

$$z_j = \frac{1}{2}[\eta(\xi_j + 1) + h(\xi_j - 1)], \tag{19}$$

while the particle's starting horizontal position is simply x_i, where the integer index i identifies the discrete grid points on the horizontal axis. Herein, the physical grid $\mathbf{r}_{ij} = (x_i, z_j)$, which defines the particles' starting positions, will be referred to as the 'fixed' grid. The particles themselves form a Lagrangian grid, $\mathbf{p}_{ij} = (a_i, c_j)$. For the purpose of the calculation, $a_i = x_i$ and $c_j = \xi_j$ are set at the start of each time step, $t = t_0$. This grid $\mathbf{p}_{ij}$ being attached to the moving particles will be referred to hereafter simply as the 'moving' grid.

3.2. The Lagrangian time step

To obtain the Lagrangian solution accurate to the order of Δt^2, we discretize the governing equations for horizontal vorticity (14) and the surface momentum equation (12) using the trapezoidal rule, while the density equation (4) is simply discretized as

$$\rho_{\mathbf{p}}^{t_1} = \rho_{\mathbf{p}}^{t_0} + \Delta t F(\rho) \tag{20}$$

with $t_1 = t_0 + \Delta t$. Here a diffusion term $F(\rho)$ has been added and the subscript $\mathbf{p}$ is used to label flow variables associated with a particle. Although the horizontal vorticity equation (14) can be cast in the trapezoidal form directly, the implicit terms that appear in the resulting equation are difficult to evaluate.

To circumvent this problem, a different approach is adopted to achieve the trapezoidal integration. The somewhat lengthy development of the approach and the finite-difference equations used are detailed in Appendix A.

The free-surface momentum equation (12) is cast in the trapezoidal form directly

$$(\mathbf{u}_\mathbf{p})_\eta^{t_1} + \frac{\Delta t}{2}\mathbf{f}\times(\mathbf{u}_\mathbf{p})_\eta^{t_1} = (\mathbf{u}_\mathbf{p})_\eta^{t_0} - \frac{\Delta t}{2}\mathbf{f}\times(\mathbf{u}_\mathbf{p})_\eta^{t_0} - \frac{g\Delta t}{2\rho_0}\left[(\rho_\mathbf{p})_\eta^{t_0}\left(\frac{\partial \eta_\mathbf{p}}{\partial x}\right)^{t_0} + (\rho_\mathbf{p})_\eta^{t_1}\left(\frac{\partial \eta_\mathbf{p}}{\partial x}\right)^{t_1}\right] + \Delta t F(\mathbf{u}_\eta), \tag{21}$$

where $\mathbf{u}_\mathbf{p} = (u_\mathbf{p}, v_\mathbf{p})$. In (21) the free surface height, $\eta_\mathbf{p}^{t_1} = z_\mathbf{p}^{t_1}(\xi = 1)$, at t_1 is obtained from the particle displacement calculation and is thus known, while $(\rho_\mathbf{p})_\eta^{t_1}$ is known from the density given by (20). For the numerical calculation in this paper, the dissipation term $F(\mathbf{u}_\eta)$ uses the operator

$$F = \nu_x\frac{\partial^2}{\partial x^2} + \nu_z\frac{\partial^2}{\partial z^2} \tag{22}$$

same also for vorticity and density diffusion in (14) and (20), where ν_x and ν_z are the numerical horizontal and vertical diffusivities/viscosities, respectively; the viscosity and diffusivity values are assumed to be the same in this paper. $F(\mathbf{u}_\eta)$ is evaluated explicitly at the free surface. Thus, all the terms on the right-hand side of (21) are now known, and $(\mathbf{u}_\mathbf{p})_\eta^{t_1}$ is determined. For vorticity and density diffusion, the horizontal part of the operator (22) is calculated explicitly at t_0, while the vertical part is usually solved implicitly at t_1 on the fixed grid after the interpolation from the moving grid.

The particle's position $(x_\mathbf{p}^{t_1}, z_\mathbf{p}^{t_1})$ at which the Lagrangian solutions of $\rho_\mathbf{p}^{t_1}$, $\mathbf{s}_\mathbf{p}^{t_1}$, and $(\mathbf{u}_\mathbf{p})_\eta^{t_1}$ are obtained can be calculated to Δt^2 accuracy if the particle acceleration is known. Except at the free surface where the surface height gradient at t_0 can be used in the surface momentum equation (12) to obtain surface particle acceleration, the acceleration in general is not calculated in the present vorticity formulation. In order to obtain the particle's position to second order accuracy, without reference to acceleration, the following scheme is used. Basically, it resorts to the approximation that

$$\left(\frac{\partial \mathbf{u}}{\partial z}\right)_\mathbf{p}^{t_1} \approx \mathbf{s}_\mathbf{p}'^{t_1} - \left(\frac{\partial w}{\partial x}\right)_\mathbf{p}^{t_0}, \tag{23}$$

where the vorticity components, s_x and s_y, in $\mathbf{s}_\mathbf{p}'^{t_1}$ are estimated from (14) with a simple forward Euler time step. Thus, the mean shear is

$$\overline{\frac{\partial \mathbf{u}}{\partial z}} = \frac{1}{2}\left[\left(\frac{\partial \mathbf{u}}{\partial z}\right)_\mathbf{p}^{t_0} + \left(\frac{\partial \mathbf{u}}{\partial z}\right)_\mathbf{p}^{t_1}\right]. \tag{24}$$

Then for the Δt step, the average horizontal and vertical velocities are approximately

$$\bar{\mathbf{u}}(z) = \bar{\mathbf{u}}_\eta - \int_z^\eta \overline{\frac{\partial \mathbf{u}}{\partial z}}\,\mathrm{d}z' \quad \text{and} \quad \bar{w}(z) = -\int_{-h}^z \frac{\partial \bar{u}}{\partial x}\,\mathrm{d}z', \tag{25}$$

where $\bar{\mathbf{u}}_\eta = (1/2)[(\mathbf{u}_\mathbf{p})_\eta^{t_1} + (\mathbf{u}_\mathbf{p})_\eta^{t_0}]$, and $(\mathbf{u}_\mathbf{p})_\eta^{t_1}$ is given by (21). Note that (21) at the free surface can be evaluated independent of the motion elsewhere because, as already noted, the surface height gradient at t_1 in (21) can be computed from the free surface particle displacement. Since (25) is accurate at least to the order of Δt, the particle displacement below the free surface given by $(x,z)_\mathbf{p}^{t_1} = (x,z)_\mathbf{p}^{t_0} + (\bar{\mathbf{u}}, \bar{w})\Delta t$ is second order accurate. This approach works well as long as $\partial\bar{\mathbf{u}}/\partial z$ is the dominant term in $\mathbf{s}'$. But, if more accuracy is needed, then the particle acceleration has to be computed, which means that the pressure P in the

momentum equation (2) has to be known a priori. We describe in Section 3.5 how P may be obtained within the present vorticity formulation.

3.3. The split-mode time integration

Because it is impractical to carry out the entire computation in the small time steps that are needed to resolve surface gravity waves, it is assumed that the slower varying $\mathbf{s}$ and ρ fields are approximately constant over the small $\Delta\tau$ steps over which surface u and η are integrated. Thus, only the surface u and η are integrated in small steps $\Delta\tau = \Delta t/n$ from t_0 to $t_1 = t_0 + \Delta t$, where the integer $n \gg 1$, while $\mathbf{s}$ and ρ are updated in one large Δt step from t_0 to t_1. This is essentially the split-mode computation strategy that has been discussed in the literature [15,16]. This approach, however, tends to excite short scale ($\sim h$ or less) surface waves, which must be filtered out periodically if the grid spacing is less than h. The alternative is to solve the surface motion implicitly without regard to the high frequency surface gravity waves. This has also been discussed in the literature, e.g. [4]. A possible implicit scheme for use with the semi-Lagrangian calculation is indicated in Appendix B.

The small time-step integration of the surface motion is treated in a Lagrangian fashion; that is the surface particles are displaced continuously in time for $n \cdot \Delta\tau$ steps. Only at the end of the multi-steps, $n \cdot \Delta\tau = \Delta t$ is the interpolation of surface velocity and η carried out, along with the interpolation of $\mathbf{s}$ and ρ. The multi-step surface time integration uses a Runge–Kutta scheme.

3.4. Interpolation back to the fixed grid

The interpolation of η, $\mathbf{s}_{\mathbf{p}}^{t_1}$, $(\mathbf{u}_{\mathbf{p}})_{\eta}^{t_1}$ and $\rho_{\mathbf{p}}^{t_1}$ from the moving grid to the fixed grid is done sequentially along each spatial dimension similar to the so-called cascade method [17]. The finite-difference interpolation weights are generated using Fornberg's algorithm [18]. This efficient and flexible algorithm is also used to generate the weights for differencing the spatial derivatives. The interpolation and spatial differentiation are typically obtained with fifth and sixth order accuracy, respectively.

3.5. The (u, w) solution and pressure

Let the flow variables on the fixed grid after the interpolation be labeled by the subscript $\mathbf{r}$. The interpolated vorticity on the fixed grid is thus $\mathbf{s}_{\mathbf{r}}^{t_1}$, with which, $\mathbf{s}_{\mathbf{r}}^{\prime t_1} = (s_y, -s_x)_{\mathbf{r}}^{t_1}$ can be formed and used in the elliptic equation (7) to obtain $w_{\mathbf{r}}^{t_1}$. To solve the elliptic equation, four boundary conditions are needed: at the surface $z = \eta$, the boundary condition can be obtained from $(\mathbf{u}_{\mathbf{r}})_{\eta}^{t_1}$ using the continuity equation

$$\left(\frac{\partial w_{\mathbf{r}}}{\partial z}\right)_{\eta}^{t_1} = -\frac{\partial}{\partial x}(u_{\mathbf{r}})_{\eta}^{t_1}. \tag{26}$$

The boundary condition at the impermeable bottom, $z = -h$, is

$$(w_{\mathbf{r}})_{-h}^{t_1} = -(u_{\mathbf{r}})_{-h}^{t_1}\frac{\partial h}{\partial x}, \tag{27}$$

where $(u_{\mathbf{r}})_{-h}^{t_1}$ is set equal to $\bar{u}(z = -h)$ from (25). In the case of a no-slip bottom, the boundary condition reduces to

$$(w_{\mathbf{r}})_{-h}^{t_1} = 0. \tag{28}$$

The two side-wall boundary conditions for w depend on the problem under consideration and may be Neumann- or Dirichlet-type, e.g., $\partial w/\partial x = 0$ at a free-slip vertical sidewall, or $w = 0$ at a no-slip sidewall.

With the boundary conditions specified as above, the elliptic equation (7) can be inverted for $w_{\mathbf{r}}^{t_1}$ on the regularly spaced fixed grid $\mathbf{r}_{ij}$,. For irregular domain geometry, we use the second order finite-difference MUD2CR routine in the MUDPACK library available from NCAR [19] to solve (7). In some of our calculations where the computation domain is essentially rectangular, the Fourier/Chebyshev transform method is also used.

Once $w_{\mathbf{r}}^{t_1}$ is determined from (7) on the fixed grid, $\mathbf{u}_{\mathbf{r}}^{t_1}$ is readily obtained from (5) by integrating downward from the surface with $(\mathbf{u}_{\mathbf{r}})_{\eta}^{t_1}$ as the boundary condition. We use the cosine grid and the Chebyshev polynomials for the vertical integration of (5) and (25) as well as for the implicit solution of vertical dissipation/diffusion terms.

When the weakly non-hydrostatic approximation is applicable, (15) is inverted for flow velocity rather than (7). Here the inversion is done on the fixed grid $\mathbf{r}_{ij}$ using second order finite-differences for the derivatives. The horizontal x-component velocity $u_{\mathbf{r}}^{t_1}$ is obtained from (16) using the solution of (15), while the y-component $v_{\mathbf{r}}^{t_1}$ is obtained simply by vertically integrating (5) since $\partial w/\partial y = 0$ in the two-dimensional case. The vertical velocity $w_{\mathbf{r}}^{t_1}$ is then obtained by integrating (17); for this vertical integration, the cosine grid and the method of Chebyshev polynomials are used as well.

At this stage, the calculation of one time step is essentially complete, and the next new Lagrangian step may begin from a new set of particles on the fixed grid. In this semi-Lagrangian solution procedure the pressure P is not computed since it is not needed. Nevertheless, P is derivable from the solution of the velocity field, and can be used, if necessary, to calculate the particle acceleration needed to improve the particle's displacement calculation, as noted in Section 3.2. To obtain P, the w momentum equation may be discretized in the trapezoidal form

$$w_{\mathbf{p}}^{t_1} = w_{\mathbf{p}}^{t_0} + \frac{\Delta t}{2\rho_0}\left[\left(\frac{\partial P}{\partial z}\right)_{\mathbf{p}}^{t_0} + \left(\frac{\partial P}{\partial z}\right)_{\mathbf{p}}^{t_1}\right] - \frac{g\Delta t}{2\rho_0}\left(\rho_{\mathbf{p}}^{t_0} + \rho_{\mathbf{p}}^{t_1}\right) + \Delta t F(w). \tag{29}$$

In this equation, the vertical velocity and density are known at both t_1 and t_0, the pressure gradient is known at t_0, and the dissipation term can be evaluated with the calculated w velocity. Thus, (29) can be solved for $(\partial P/\partial z)_{\mathbf{p}}^{t_1}$. The P is then obtained by interpolating $(\partial P/\partial z)_{\mathbf{p}}^{t_1}$ to the fixed grid $\mathbf{r}_{ij}$ and integrating vertically, with the surface atmospheric pressure as the boundary condition.

4. Validation tests

To test the numerical model, three exact nonlinear solutions of the DJL equation are used as benchmarks. They are finite-amplitude periodic internal gravity waves, internal solitary waves, and stratified flow over a ridge. The DJL equation describes the motion of a finite-amplitude density perturbation propagating at a constant speed or a stationary disturbance in a steady stream. A useful reference on this equation's derivation, generalization, and applications can be found in [12]. Also a recent alternative variational approach is given in [20]. For the purpose here, the equation is of the form

$$\left(\frac{\partial^2\phi}{\partial x^2} + \frac{\partial^2\phi}{\partial z^2}\right) + \frac{1}{\rho}\frac{\mathrm{d}\rho(\psi)}{\mathrm{d}\psi}\left\{\frac{1}{2}\left[\left(\frac{\partial\phi}{\partial x}\right)^2 + \left(\frac{\partial\phi}{\partial z}\right)^2 + 2c\frac{\partial\phi}{\partial z}\right] - \frac{g\phi}{c}\right\} = 0, \tag{30}$$

where ψ and ϕ are the streamfunctions in the moving and stationary frames of reference, respectively, and are related by c, the disturbance's propagation speed, as $\psi = \phi + cz$; the horizontal velocity in the stationary frame is thus $u = \partial\phi/\partial z = \partial\psi/\partial z - c$, and the vertical velocity $w = -\partial\phi/\partial x = -\partial\psi/\partial x$.

It is possible to write $\rho(\psi) = \rho_0[1 - \sigma B(\psi)]$, where $\sigma = \Delta\rho/\rho_0$ is the total density difference between the top and bottom boundaries normalized by the constant reference density ρ_0. To be consistent with the

Boussinesq approximation of the density effect in the momentum equations, it is assumed that $\sigma \ll 1$ so that all terms of σ^2 and higher in (30) can be omitted. The DJL equation then reduces to

$$\left(\mu^2 \frac{\partial^2 \phi}{\partial x^2} + \frac{\partial^2 \phi}{\partial z^2}\right) + \frac{1}{\hat{c}^2} \frac{\partial B(\phi + z)}{\partial(\phi + z)} \phi = 0. \tag{31}$$

The above reduced DJL equation has now been cast in the standard non-dimensional form [21], where ϕ and ψ have been scaled by $c \cdot h, x$ by $k^{-1} = L/2\pi$, and z by h, and the dimensionless phase speed is $\hat{c} = c/\sqrt{\sigma g h}$. All comparisons with the solutions of the DJL equation (31) in this section are presented in terms of dimensionless variables as defined above (n.b. all variables are dimensionless in this section only). The parameter μ appears in (31) as part of scaling but plays no role in the determination of ϕ here.

The known solutions of this equation typically have been obtained assuming a fluid domain bounded by a flat rigid upper surface. In the free surface model nearly the same rigid/flat surface effect can be achieved by using a large gravitational constant. The simulation results to be shown here for the validation of the free surface model all have been obtained using $g \geqslant 980$ m/s^2, specifically, in the time integration of (21).

4.1. Periodic internal gravity waves

For a linear density stratification, $\partial B/\partial \psi = 1$, and (31) has the first mode internal gravity wave solution

$$\phi = A \cos(x - \hat{c}t) \sin(\pi z) \quad \text{for } 0 = z = 1 \tag{32}$$

and

$$\hat{c} = (\mu^2 + \pi^2)^{-1/2}. \tag{33}$$

The horizontal and vertical velocities given by (32) are

$$u = \pi A \cos(x - \hat{c}t) \cos(\pi z), \tag{34a}$$

$$w = A \sin(x - \hat{c}t) \sin(\pi z). \tag{34b}$$

Density perturbation consistent with this propagating wave is

$$\rho' = \frac{A}{\hat{c}} \cos(x - \hat{c}t) \sin(\pi z) \tag{35a}$$

and the total density is

$$\rho = 1 - z + \rho'. \tag{35b}$$

Here the dimensionless variables u, w, ρ, ρ', and t have been scaled as follows: u by c, w by μc, with $c = \hat{c}\sqrt{\sigma g h}$, ρ and ρ' by $\Delta\rho$, the total density difference, and t by $(\mu\sqrt{\sigma g/h})^{-1}$.

The free surface model is initialized at $t = 0$ using the above u, w and ρ'. Two examples of initial flow fields ϕ and ρ are shown in Figs. 1(a) and (b) corresponding to amplitudes $u_0 = \pi A < 1$ and $u_0 > 1$, respectively. In the case of $u_0 > 1$, recirculation zones appear in the density field as a consequence of the local wave particle speed exceeding the wave phase speed, recalling that u has been scaled by c.

The periodic internal waves are simulated for three different amplitudes, $u_0 = 0.16$, 0.32, and 1.6 and for a range of μ between 0.1 and 5. The simulations were performed alternately using the weakly and then the

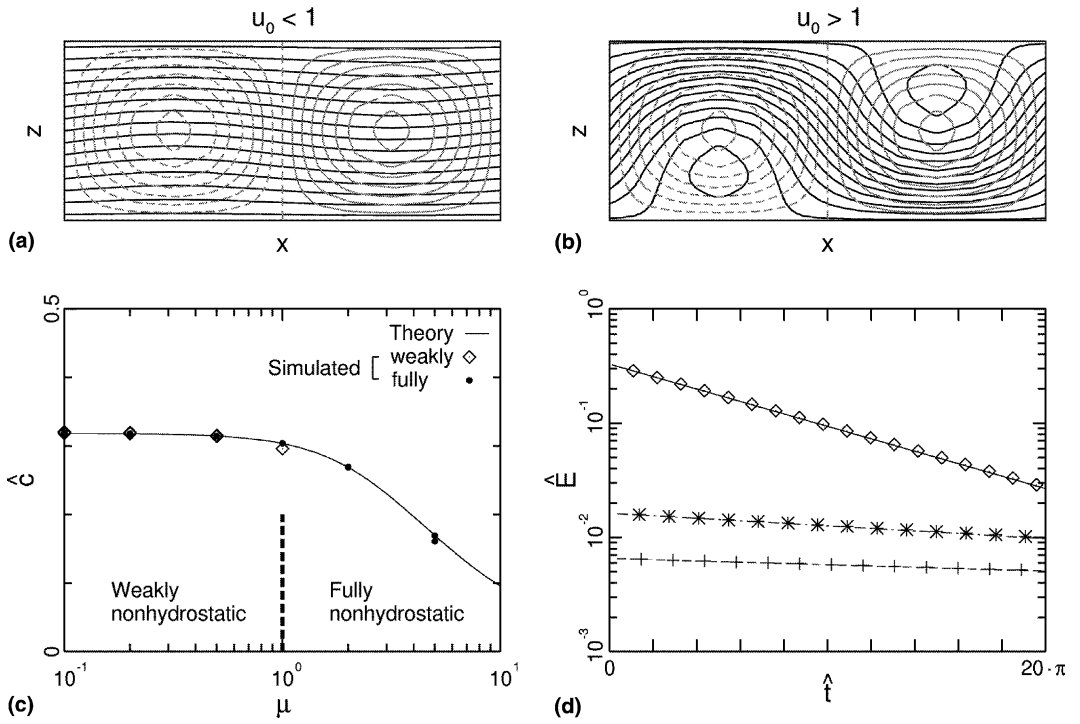

Fig. 1. Periodic internal gravity wave case. (a) Small amplitude wave example, u_0 (= particle speed normalized by phase speed) <1; density contours (solid); streamlines (grey solid – positive; dashed – negative). (b) Large amplitude wave example, $u_0 > 1$. (c) Comparison of theoretical phase speeds (solid curve) and simulated wave phase speeds (symbols). The simulation results at each μ are obtained from runs with and without viscosity/diffusivity and for three different amplitudes $u_0 = 0.16$, 0.32, and 1.6. The results are all plotted but are indistinguishable as they overlap. (d) Energy decay versus time. Predicted (lines) and simulated (symbols). Only the weakly non-hydrostatic simulation results are shown.

fully non-hydrostatic equations. For the weakly non-hydrostatic calculation, the resolution is limited to Δx not less than one, which corresponds to dimensionally a grid spacing not less than the local depth, h. The surface time step $\Delta\tau$ is $\sim$ a tenth of $\Delta x/\sqrt{gh}$ while $\Delta t \sim 100\Delta\tau$. A range of dimensionless viscosity/diffusivity values are considered, $0 \leqslant v_x \leqslant 0.224$ and $0 \leqslant v_z \leqslant 0.0393$.

The phase speed $\hat{c}$ as a function of μ calculated from the simulated internal wave field is shown in Fig. 1(c), where the theoretical speed (solid curve) given by (33) is also plotted. For small μ, i.e., wavelength greater than water depth, the weakly non-hydrostatic equations are applicable. In the range of $\mu < 1$, all simulations with and without dissipation using weakly non-hydrostatic approximation obtain phase speeds that agree with the theoretical result, and this is so despite the fact that the approximation is valid strictly for $\mu \ll 1$. No result is shown beyond $\mu = 1$ as this approaches the resolution limit of the grid spacing, which is to be not less than h as noted above. The fully non-hydrostatic simulations obtain phase speeds that agree with the theory over a broader range, to $\mu = 5$, where the ratio of the actual wavelength to the water depth is close to one. For ratios greater than this, the approximation, (23)–(25), for the displacement calculation is inapplicable, as $\partial w/\partial x$ now can be as large as $\partial u/\partial z$, and no additional result is obtained.

Fig. 1(d) compares the simulation time series for the wave energy to the theoretical prediction. In the presence of dissipation and diffusion, the theoretical wave energy should decay as $\exp[-2(v_x + \pi^2 v_z)t]$. The total wave energy, kinetic plus potential, per unit volume in terms of the dimensionless variables (34) and (35) is

$$E = \frac{1}{2}\left(u^2 + \mu^2 w^2 + \left(\frac{\rho'}{\hat{c}}\right)^2\right). \tag{36}$$

Fig. 1(d) shows that the total energy $\hat{E}$, summing E over the volume, decays with time at a rate consistent with that given by the theory (straight lines). The results are shown for $\mu = 0.5$ to test the weakly non-hydrostatic calculation and for three different pairs of v_x and v_z.

4.2. Internal solitary waves

Fully nonlinear, finite-amplitude internal solitary gravity wave solutions can be obtained from (31) by requiring ϕ to vanish as $x \to \pm\infty$. Such finite-amplitude solutions, however, have to be determined generally by numerical means, as (31) is a nonlinear eigenvalue problem with the eigenvalue, the inverse of the squared phase speed $\hat{c}$, to be determined with the unknown ϕ. The numerical solution of the solitary wave problem has been investigated by several researchers [20–22]. Here, for testing the free-surface non-hydrostatic model, we will use the solitary wave solutions given in [20] that apply to the density profile, $\rho(\psi) = \rho_0[1 - \sigma\tanh(\beta\psi)]$, where $0 \leqslant \psi \leqslant 1$, and $1/\beta$ times h is the half width of the tanh function; thus in (31), $B(\psi) = \tanh(\beta\psi)$. Moreover, since there is no fixed horizontal scale for the solitary wave, h is used for $1/k$ with $\mu = 1$ in (31).

Shown in Fig. 2(a) is the solution for $\beta = 1$ and $\hat{c} = 0.294$. For this stratification, the far field density varies almost linearly with respect to z. The solitary wave appears as a single wave of elevation with the lines of constant density (isopycnals) displaced upward. (A mirror image of a solitary wave of depression exists for $-1 \leqslant \psi \leqslant 0$.) Shown in Fig. 2(b) is the solution for the same stratification but for a larger wave amplitude, and $\hat{c} = 0.302$. This case has a maximum fluid particle speed comparable to the wave's phase speed near the bottom boundary. Figs. 2(c) and (d) show the solitary wave solutions for $\beta = 4$. The density stratification is now mostly limited to the lower half of the domain. The largest amplitude solitary wave, $\hat{c} = 0.431$, Fig. 2(d), contains a recirculation core, in which the particle speed exceeds the phase speed. The solitary waves in all four plots are displayed with the same vertical-to-horizontal ratio of 1:20 to contrast the difference in their sizes. The horizontal extent of the contour lines marks the actual extent of the computational domain. The DJL solutions in Figs. 2(a)–(c) are used as the benchmarks for testing the weakly non-hydrostatic calculations. The larger amplitude wave in Fig. 2(b) presents a more challenging test as the scale of flow variation is close to the limit of the weakly non-hydrostatic approximation. The largest amplitude case with a recirculation core in Fig. 2(d) is fully non-hydrostatic and is used to test the fully non-hydrostatic calculation.

The simulated solitary waves initialized with the density and velocity of the DJL solitary waves in Figs. 2(a)–(d) are shown in corresponding Figs. 2(e)–(h). A periodic horizontal boundary condition is used in all the calculations. The solitary waves shown have been integrated for approximately 10 buoyancy periods, during which time, these solitary waves have traveled through the box at least once; for plotting, they have been repositioned to near the center of the domain so that they are easily compared with the DJL solutions in Figs. 2(a)–(d). A slight viscosity/diffusivity has been used in the two large amplitude cases to maintain numerical stability, $v_x = 2.2 \times 10^{-5}$ and $v_z = 2.0 \times 10^{-6}$ for the case in Fig. 2(f) and $v_x = 2.9 \times 10^{-4}$ and $v_z = 2.9 \times 10^{-5}$ for the case in Fig. 2(h). The two weak amplitude cases tend to be numerically stable even without viscosity; nevertheless these two cases have also been run with small viscosity/diffusivity similar to the values above.

The simulated solitary waves in Figs. 2(e)–(g) using the weakly non-hydrostatic equations are in good agreement with the benchmark solitary wave solutions in Figs. 2(a)–(c), except for minor disturbance away from the solitary waves. The weak disturbance appears to be on both sides of the solitary waves because of the periodic boundary condition. The horizontal resolution is limited to $\Delta x/h \geqslant 1$. In the vertical direction

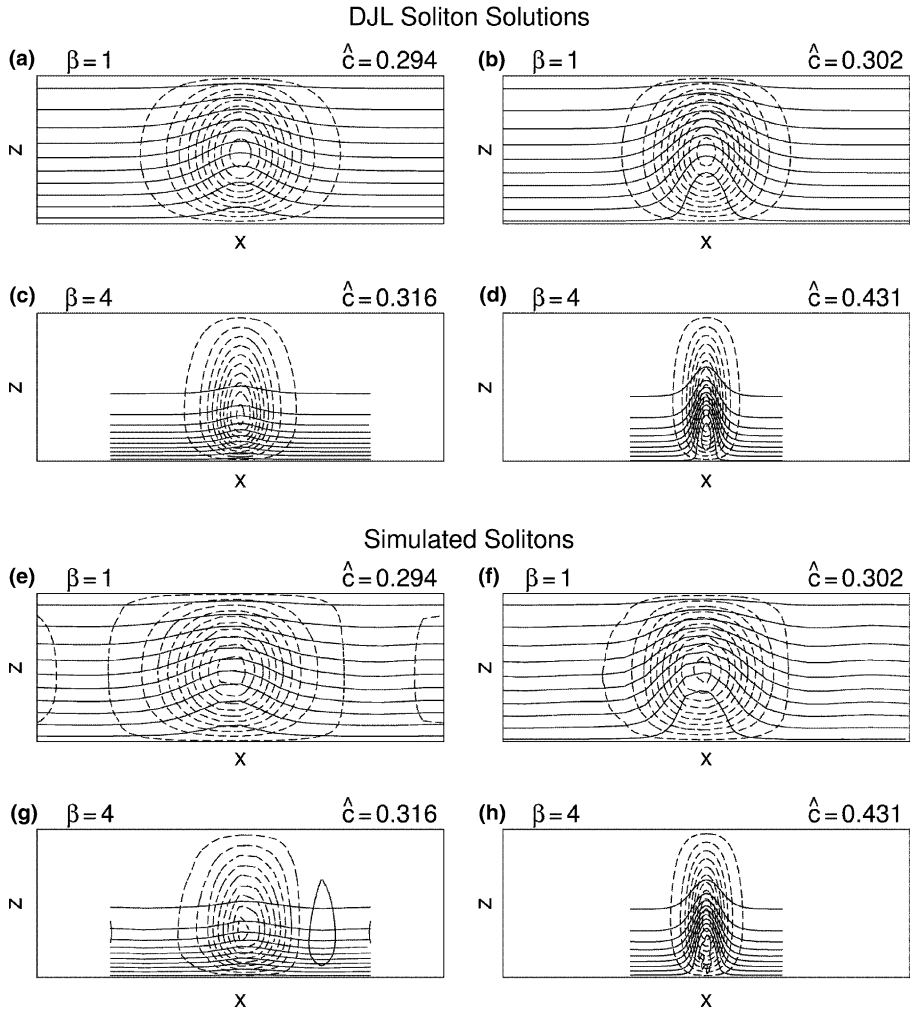

Fig. 2. Internal solitary waves. Streamline contours – dashed; density contours – solid. (a)–(d) JDL solutions. (e)–(g) Simulations. The solitary wave, propagating from right to left, has been repositioned to the center of each plot for ease of comparison. The simulation results are all shown at the time of ~10 buoyancy periods. All plots have the same 1:20 aspect ratio. The actual computation domain is given by the horizontal extent of the contour lines.

the motion is resolved with a 33-point cosine grid. The finite-difference interpolation is used for the small amplitude cases in Fig. 2(e) and (g). A spectrally accurate interpolation is used for the higher amplitude case in Fig. 2(f). The more accurate spectral interpolation is necessary to compensate for the limited resolution $\Delta x \sim h$ which marginally resolves the solitary wave. The largest amplitude case, Fig. 2(h), which is simulated using the fully non-hydrostatic equations, is resolved with 65 vertical grid points and 160 horizontal grid points and interpolated using finite-difference; but the inversion of the elliptic equation (7) is done spectrally. Again the comparison with the benchmark case, Fig. 2(d), is favorable.

In Figs. 3(a) and (b) the horizontal position of the simulated solitary wave, defined by the position of the amplitude maximum, is plotted as a function of time for the four cases, as well as the predictions (straight lines) given by the benchmark solutions. For this plot, $x' = c't'$, where $x' = x\beta$, $t' = t\sqrt{\beta}$ and $c' = \hat{c}\sqrt{\beta}$; the

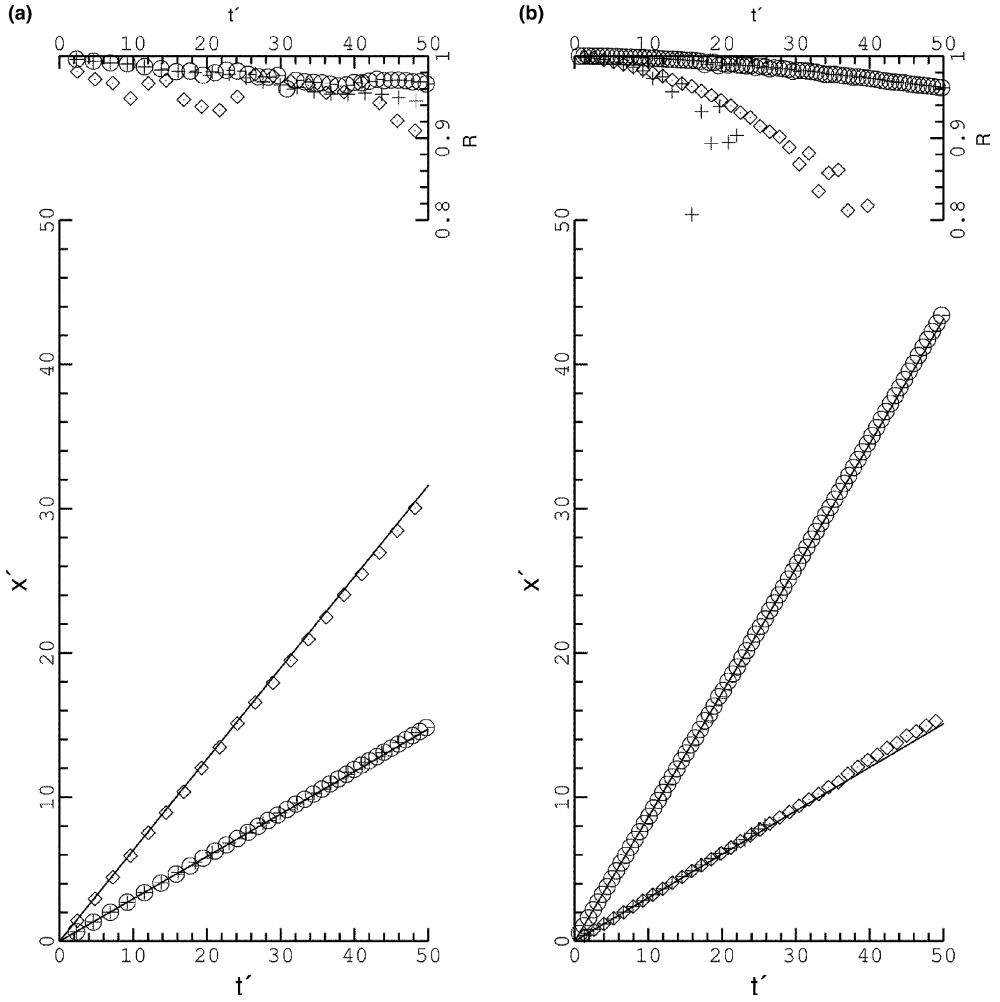

Fig. 3. Comparison of the predicted (line) and simulated (symbols) solitary wave positions x' as a function of time t' and the similarity, as measured by the correlation coefficient R, between the simulated wave and the DJL solution. t' has the unit of buoyancy periods, and x' is given in the unit of the density-interface thickness. The symbols correspond to the cases in Fig. 2 as follows: (a) ♢, Fig. 2(g); +, Fig. 2(e), and ◯ same but without viscosity. (b) ◯, Fig. 2(h); ♢, Fig. 2(f), and + same but without viscosity.

addition of the multiplicative factor β accounts for the fact that the relevant height scale for the solitary wave is the stratification scale h/β. Above the x' vs. t' plot is the correlation coefficient, R, which measures the degree of similarity between the simulated and benchmark DJL solitary wave streamfunctions, plotted as a function of time. In Fig. 3(a), the line of larger slope is the predicted x' vs. t' for the solitary wave case in Fig. 2(c), and the symbols are the locations from the numerical simulation. This simulation is inviscid and weakly non-hydrostatic, and the predicted and simulated positions are seen in agreement over the 50 buoyancy periods plotted. The shape of the simulated wave also agrees closely with the DJL solution as indicated by $R > 0.9$ over the same time period. The line of smaller slope in Fig. 3(a) is the prediction for the weakly non-hydrostatic case in Fig. 2(e), and again there is an agreement between the simulated and predicted positions. Two simulation results are shown in this comparison, one with and one without viscosity/diffusivity. Although both compare well with the prediction, the one with viscosity performs slightly

poorer with R decreasing to 0.94. In Fig. 3(b), the larger slope line is the prediction for the fully non-hydrostatic case in Fig. 2(h), and the simulated wave positions follow this line closely. The correlation plot indicates a good agreement between the simulated solitary wave and the DJL solution; nevertheless, the correlation decreases slowly with time to $\sim$0.95 at $t' = 50$ buoyancy periods. The smaller slope line in Fig. 3(b) is the prediction for the weakly non-hydrostatic case in Fig. 2(b), and the simulation results for the wave positions shown are obtained with and without viscosity/diffusivity. The inviscid result terminates at around $t' = 25$, at which point the run has become noise, and this is evident in the loss of the correlation in the R vs. t' plot. The viscous result continues for a longer time. But it can be seen that the simulated wave position departs gradually from the prediction with increasing t', and the correlation becomes poor. For this weakly non-hydrostatic case, the resolution of the solitary wave is only marginal as noted earlier in this section.

4.3. Density-stratified flow over a ridge

Solutions of stratified flow over a barrier can be determined from the DJL equation in a number of ways [12,23]. Here, we will use a simple approach, by exploiting the fact that streamlines and isopycnals are coincident in the moving frame of reference of a solitary wave. In this reference frame, a uniform current now appears in the far field, moving at a constant speed c, and the solitary wave is a local disturbance to this current. Since the streamlines and isopycnals are now coincident, they must be disturbed in the same manner across the solitary wave. In the case of a solitary wave of elevation considered in Section 4.2, the disturbance appears as an upward deflection or a hump for the isopycnals, and this is now true as well for the streamlines. By picking one such deflected streamline or isopycnal and treating it as a solid surface, a solution for a flow over a ridge is then obtained. The Froude number for such a flow is necessarily supercritical.

Fig. 4(a) shows the streamlines of a flow over a ridge obtained using the above procedure. The ridge has a maximum slope of 0.04, and the domain's aspect ratio $h/L = 1/60$. Superimposed in the same figure are the streamlines of simulated flow obtained using the weakly non-hydrostatic equations without viscosity/diffusivity. The simulated flow is shown at 50 buoyancy periods after the start. As is evident, the simulated and the theoretical streamlines are indistinguishable, confirming the validity of (15) and (16) for variable h. Fig. 4(b) shows the simulated streamlines from the inviscid fully non-hydrostatic calculation and the superimposed theoretical streamlines. Again the simulated and the theoretical streamlines are indistinguishable. In Fig. 4(c), the flow over a steeper ridge with a slope of 0.244 is shown. The theoretical streamlines are the dashed curves and the simulated streamlines are solid. The simulation is fully non-hydrostatic, and to maintain numerical stability, a horizontal viscosity/diffusivity of $v_x = 2.25 \times 10^{-3}$ is used, and $v_z = 0$. This dissipation accounts for the small reduction of the transport after $\sim$50 buoyancy periods, the time at which the plot is shown; the reduction is indicated by the solid curves being slightly higher than the dashed curves; the contour interval is the same for both the theoretical and the simulated streamfunctions.

5. Simulation of the tidal generation of internal solitary waves

One possible application of the present free-surface non-hydrostatic model is the simulation of coastal internal solitary waves. These waves are prominent features on the continental shelf and are detected frequently in spaceborne radar images of the sea surface; some examples can be found in [24–27]. Their origin can be usually traced to the ocean tides at the continental shelf-break. The rapid depth change across this region causes tidal currents to contract and expand, producing large thermocline oscillations that propagate onshore as solitary wave trains.

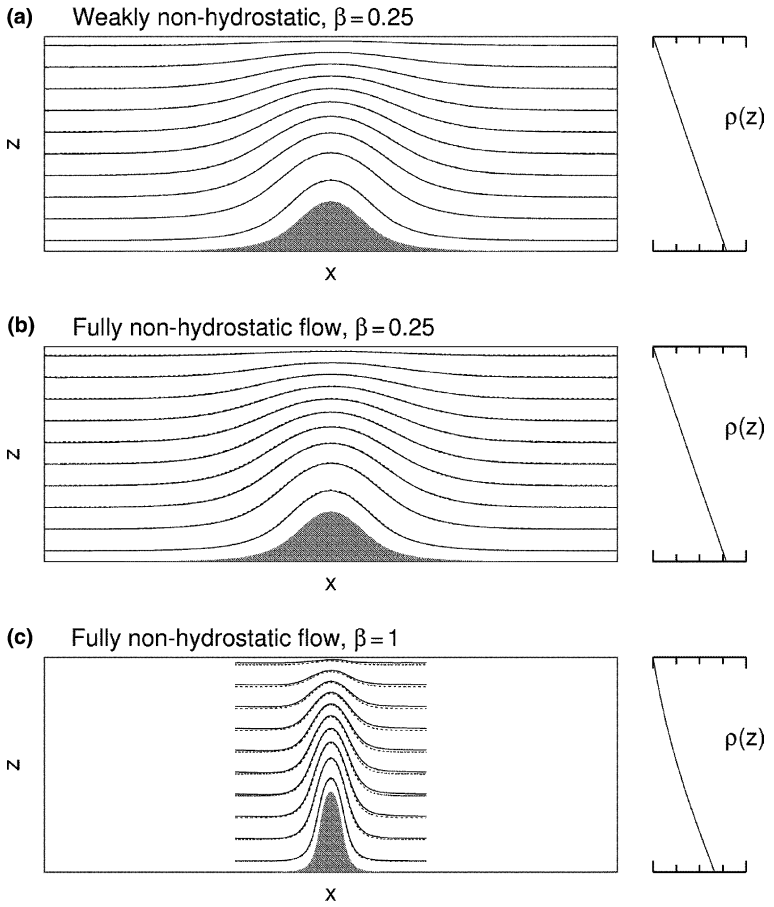

Fig. 4. Flow over a ridge. Simulated streamlines – solid; theoretical streamlines – dashed. The current flows from left to right. The far-field density as a function of z is shown with the line profile on the right-hand side; the horizontal density axis is equivalent to the parameter $\sigma = \Delta\rho/\rho_0$ with $\sigma = 10^{-4}$/tick mark. The contour plots are shown with a common aspect ratio of 1:60 and at a time of $\sim$50 buoyancy periods. (a) and (b) The maximum ridge slope is 0.04. (c) The maximum ridge slope is 0.24. The horizontal extent of the simulation domain corresponds to that of the streamlines.

There have been a number of numerical simulation studies of internal solitary waves [28–32]. Here the canonical problem of tidal generation of internal solitary waves at the shelf-break will be considered to demonstrate the applicability of the present free-surface hydrodynamic model, in particular, its applicability with respect to the weakly non-hydrostatic approximation. It may be noted that the present model with the weakly non-hydrostatic approximation takes into account the full range of physics, namely, free surface tides, continuous density stratification, Coriolis force, variable bathymetry, and dissipation, which is only partially considered in the literature cited above.

For this canonical problem, the shelf-break topography may be idealized as a tanh function. The mean density stratification may be assumed horizontally uniform, and the tides may be represented by an oscillating free surface at the open boundary. The specific functional form chosen for the bottom topography is $h = -75\ \text{m} - 25\ \text{m} \cdot \tanh[(x - 50\ \text{km})/1.25\ \text{km}]$ for $0 \leqslant x \leqslant 100$ km. The mean density stratification, with $\Delta\rho = 4.5\ \text{kg/m}^3$ over 25 m, is approximately that observed at the Mid Atlantic Bight in a field experiment [26], where solitary wave trains have been detected. The tidal forcing is represented as $\eta = 2$

$m \cdot \sin(2\pi \cdot t/12.4\ \text{h})$ at the open boundary. The other parameter values chosen are: $g = 9.8\ \text{m/s}^2$, $f = 1.03 \times 10^{-4}$/s approximately at mid latitudes, $0.54 \leqslant v_x \leqslant 2.17\ \text{m}^2/\text{s}$ in the interior, $8.68 \leqslant v_x \leqslant 17.36\ \text{m}^2/\text{s}$ near the lateral boundaries to reduce wave reflection, and $1.12 \times 10^{-4} \leqslant v_z \leqslant 2.0 \times 10^{-4}\ \text{m}^2/\text{s}$.

The model domain is closed on the coastal side, $x = 0$, by a vertical wall, where the boundary conditions are $u = 0$, $\partial v/\partial x = 0$, $\partial w/\partial x = 0$, and $\partial \eta/\partial x = 0$. The boundary conditions on the open ocean side, $x = 100$ km, are, in addition to the tidal forcing given above, $\partial v/\partial x = 0$ and $\partial w/\partial x = 0$, but no condition imposed on u. The vertical boundary conditions are $\partial u/\partial z = 0$, $\partial v/\partial z = 0$, and $\partial \rho/\partial z = 0$ at the surface and bottom. The inversion of the weakly non-hydrostatic equation (15) uses the boundary conditions $\partial \tilde{u}/\partial x$ at $x = 100$ km and $\tilde{u} = 0$ at $x = 0$ km. Because the total water depth $H_\eta = h + \eta$ in (15) now changes with time, the finite-difference matrix representation of (15) has to be updated periodically. For the low frequency tide considered here, an update every $100\Delta t$ steps is performed.

The results of three numerical simulations with increasing horizontal resolution, $\Delta x/h_{\max} = 2, \Delta x/h_{\max} = 1$ and $\Delta x/h_{\max} = 0.5$, are shown in Figs. 5(a)–(c), respectively. The vertical grid for all three has cosine spacing with 33 grid points. The first two are weakly non-hydrostatic simulations, and the third and highest resolution one is fully non-hydrostatic. All three simulations begin from the same initial state of

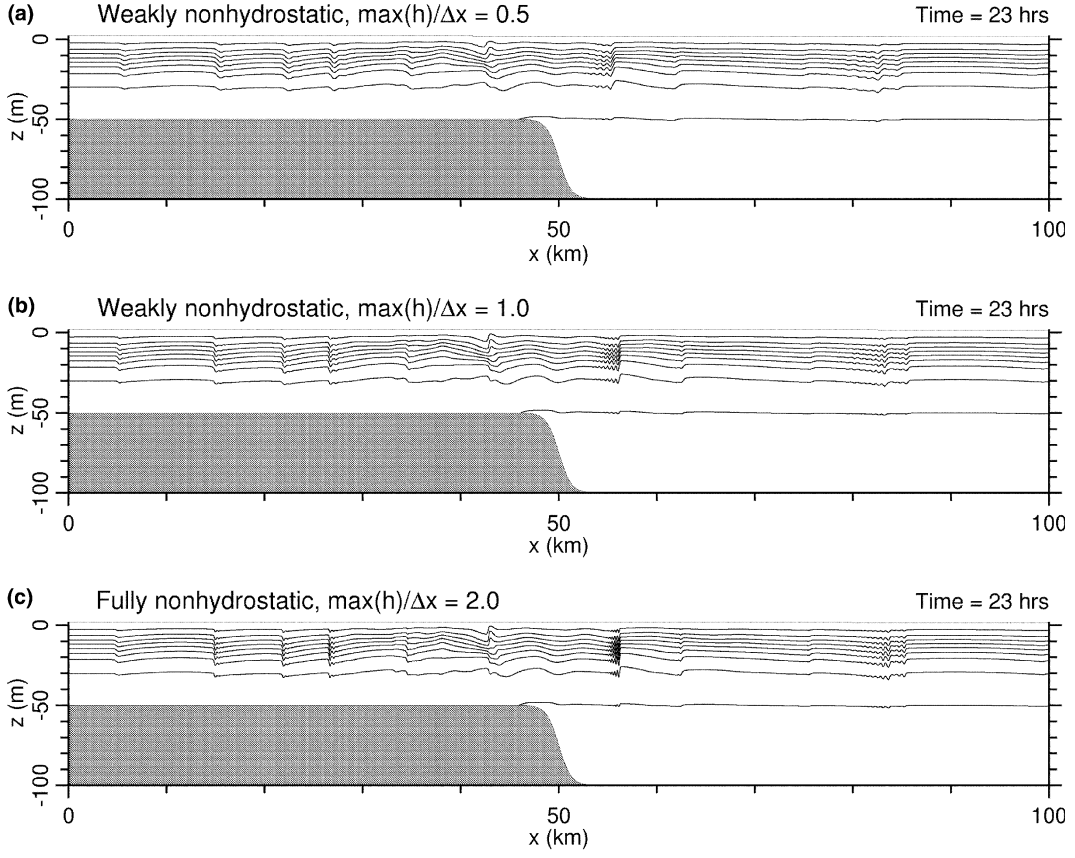

Fig. 5. Simulation of internal solitary wave trains generated at the shelf-break by the tide. The tidal forcing is applied at the right boundary. The shelf-break has a maximum slope of 0.02. The maximum depth, $\max(h)$, is 100 m. The results are shown at 23 h or 1.85 tidal cycles. (a) and (b) Horizontal resolution $\Delta x = 200$ and 100 m, respectively. These two lower resolution weakly non-hydrostatic simulations are comparable to (c), the higher resolution fully non-hydrostatic simulation with $\Delta x = 100$ m.

rest with tidal forcing at the boundary. At the time shown, multiple bore-like solitary waves have been generated and propagate in opposite directions away from the shelf-break. These solitary waves are waves of depression. Their generation and evolution are consistent with the previously published studies [29,32], to which the reader may refer for more details concerning the underlying physics; the previous studies, however, use rigid lid domains in which tidal-like currents have to be prescribed as a background flow over the whole domain. The comparison in Fig. 5 shows that the lower resolution weakly non-hydrostatic model is able to capture the field of solitary wave trains as well as the high resolution non-hydrostatic model albeit with less detail.

All three simulations have been carried out with uniform Δx. In the case of weakly non-hydrostatic simulation, because Δx can be smaller for smaller h, it is possible to use a higher resolution grid on the shelf and a lower resolution one off the shelf. The present semi-Lagrangian scheme with the flexible Fornberg's algorithm for generating interpolation/finite-difference weights is readily adaptable to a variable grid system. We have confirmed the variable grid computation separately, and expect it to be useful for addressing coastal problems. It is of interest to note that the present model formulation also lends itself readily to the embedding of a high resolution non-hydrostatic computational domain within a larger scale, lower resolution, weakly non-hydrostatic computational domain, because a consistent framework has been used here to formulate the model's weakly and the fully non-hydrostatic equations. Specifically, the time-dependent governing equations (3), (4) and (8) are the same for both the weakly (large-scale) and fully (small-scale) non-hydrostatic domains. Thus, the time integration may proceed in the same way for both domains, while at each time step the 2D and 3D elliptic equations are solved in the respective weakly and fully non-hydrostatic domains, with the boundary conditions for the embedded fully non-hydrostatic domain given by the solution of the large-scale weakly non-hydrostatic domain. This embedding capability means that in regions such as across an internal wave train where high resolution is needed, the more demanding, fully non-hydrostatic computation can be used while the more efficient weakly non-hydrostatic computation can be carried out over a broader area. This potential application, however, is yet to be investigate; in fact, there also exists the potential of adding the third, shelf-wide, hydrostatic domain, within which to embed the weakly and fully non-hydrostatic domains. The hydrostatic model, useful for shelf-wide coastal ocean circulation modeling [16], is already contained in the present formulation as noted earlier in Section 2. In such a triply nested domain, current/wave motions from shelf-scales to intermediate and fine-scales may be modeled simultaneously.

6. Summary

An alternative formulation of the free surface hydrodynamic model has been presented based on the horizontal vorticity and surface momentum equations. This formulation provides a framework for applying the weakly non-hydrostatic approximation to situations where the horizontal scale of the density-stratified wave/current motion exceeds the local water depth. The approximation eliminates the vertical dimension of the elliptic equation that is normally required for the fully non-hydrostatic calculation. This enables a more efficient computation where fully non-hydrostatic physics is not needed.

A semi-Lagrangian scheme is used for the numerical integration of the hydrodynamic model. The Lagrangian time integration is carried out explicitly in the split-mode fashion, where the particle motion associated with the fast surface gravity wave mode is integrated in small $\Delta\tau$ steps, while the motion of the slower evolving internal wave mode is integrated in larger Δt steps with $\Delta t \gg \Delta\tau$. Alternatively, the surface mode can be integrated implicitly in large Δt steps when surface wave motion is of minor importance, and this is indicated in Appendix B. After a Lagrangian time step, the efficient sequential one-dimensional method is used to interpolate the flow field back to a reference fixed grid. A relatively simple approach based on the time rate of change of velocity shear is used to provide the particle displacement calculation

accurate to the second order in time. This is, however, limited to flow having horizontal vorticity characterized by vertical u-shear greater than horizontal w-shear. To calculate the displacement field without this limitation and with greater accuracy requires additional calculation of the pressure and the acceleration field. The present solution procedure clearly needs to be improved in this direction.

The hydrodynamic model is validated using the nonlinear non-hydrostatic solutions given by the DJL equation for periodic internal gravity waves, internal solitary waves, and density-stratified flow over a ridge. These non-hydrostatic motions are simulated using the model with and without the weakly non-hydrostatic approximation. It is shown that the weakly non-hydrostatic approximation has a broader range of applicability, up to $\mu = 1$, than that expected, $\mu \ll 1$. The simulated non-hydrostatic wave/current fields agree well with the benchmark solutions. The phase speeds of simulated waves are in generally good agreement with the expected, and the flow over a ridge matches closely the expected flow. It should be noted that in these simulations the surface velocity is calculated as part of the time integration, not prescribed as a boundary condition from the known benchmark solutions, and thus, the tests here also validate the free surface calculation. Finally, a numerical simulation of tidal generation of internal solitary waves at the shelf-break has been demonstrated. It is shown that the more efficient weakly non-hydrostatic computation can capture the generation and propagation of the solitary wave trains as well as the fully non-hydrostatic computation. This result indicates that over the wide extent of coastal ocean domain, the weakly non-hydrostatic computation can be more economically utilized, while the fully non-hydrostatic computation may be embedded in a sub-region of the domain where higher resolution is needed. In modeling still larger coastal area, it is suggested that the non-hydrostatic computation may be further embedded within a larger-scale hydrostatic computation which the present model can also provide.

Acknowledgements

This work is a contribution to the Modeling Space–Time Ocean Acoustic Coherence project and the Flow Instability Patterns project at the Naval Research Laboratory, sponsored by the Office of Naval Research, and is supported in part by a grant of HPC time from the DoD HPC Shared Resource Center, CEWES.

Appendix A

The actual $(s_x)_{\mathbf{p}}^{t_1}$ and $(s_y)_{\mathbf{p}}^{t_1}$ equations used for the numerical time integration are obtained in the two-dimensional (x,z) domain as follows.

From (2), the Lagrangian momentum equations discretized in time in the trapezoidal form are

$$\frac{u_{\mathbf{p}}^{t_1} - u_{\mathbf{p}}^{t_0}}{\Delta t} = \frac{f}{2}\left(v_{\mathbf{p}}^{t_1} + v_{\mathbf{p}}^{t_0}\right) - \frac{1}{2\rho_0}\left[\frac{\partial P_{\mathbf{p}}^{t_1}}{\partial x} + \frac{\partial P_{\mathbf{p}}^{t_0}}{\partial x}\right], \tag{A.1}$$

$$\frac{v_{\mathbf{p}}^{t_1} - v_{\mathbf{p}}^{t_0}}{\Delta t} = \frac{f}{2}\left(u_{\mathbf{p}}^{t_1} + u_{\mathbf{p}}^{t_0}\right), \tag{A.2}$$

$$\frac{w_{\mathbf{p}}^{t_1} - w_{\mathbf{p}}^{t_0}}{\Delta t} = -\frac{1}{2\rho_0}\left[\frac{\partial P_{\mathbf{p}}^{t_1}}{\partial z} + \frac{\partial P_{\mathbf{p}}^{t_0}}{\partial z}\right] - \frac{g}{2\rho_0}\left(\rho_{\mathbf{p}}^{t_1} + \rho_{\mathbf{p}}^{t_0}\right). \tag{A.3}$$

Decoupling $u_{\mathbf{p}}^{t_1}$ and $v_{\mathbf{p}}^{t_1}$ from (A.1) and (A.2) by cross elimination, one obtains

$$u_{\mathbf{p}}^{t_1} = \alpha_1 u_{\mathbf{p}}^{t_0} + \alpha_2 v_{\mathbf{p}}^{t_0} - \frac{\alpha_3}{\rho_0}\left[\left(\frac{\partial P}{\partial x}\right)_{\mathbf{p}}^{t_1} + \left(\frac{\partial P}{\partial x}\right)_{\mathbf{p}}^{t_0}\right], \tag{A.4}$$

$$v_{\mathbf{p}}^{t_1} = \alpha_1 v_{\mathbf{p}}^{t_0} - \alpha_2 u_{\mathbf{p}}^{t_0} + \frac{\alpha_4}{\rho_0}\left[\left(\frac{\partial P}{\partial x}\right)_{\mathbf{p}}^{t_1} + \left(\frac{\partial P}{\partial x}\right)_{\mathbf{p}}^{t_0}\right], \tag{A.5}$$

where

$$\alpha_1 = \frac{1-\tilde{f}^2}{1+\tilde{f}^2}, \quad \alpha_2 = \frac{2\tilde{f}}{1+\tilde{f}^2}, \quad \alpha_3 = \frac{\Delta t}{2(1+\tilde{f}^2)}, \quad \alpha_4 = \tilde{f}\,\alpha_3 \quad \text{and} \quad \tilde{f} = \frac{f\,\Delta t}{2}.$$

With $\partial w/\partial y = 0$, $(s_x)_{\mathbf{p}}^{t_1}$ obtained through differentiating (A.5) with respect to z is

$$(s_x)_{\mathbf{p}}^{t_1} = -\frac{\partial v_{\mathbf{p}}^{t_1}}{\partial z} = -\alpha_1 \frac{\partial v_{\mathbf{p}}^{t_0}}{\partial z} + \alpha_2 \frac{\partial u_{\mathbf{p}}^{t_0}}{\partial z} - \frac{\alpha_4}{\rho_0}\frac{\partial}{\partial z}\left[\left(\frac{\partial P}{\partial x}\right)_{\mathbf{p}}^{t_1} + \left(\frac{\partial P}{\partial x}\right)_{\mathbf{p}}^{t_0}\right]. \tag{A.6}$$

Here all the flow variables are Lagrangian variables and are functions of the Lagrangian coordinates (a, c), and the differentiation with respect to z on the right-hand side of (A.6) obeys the chain rule, $\partial/\partial z = (\partial a/\partial z)(\partial/\partial a) + (\partial c/\partial z)(\partial/\partial c)$. The other vorticity component, $(s_y)_{\mathbf{p}}^{t_1} = (\partial u_{\mathbf{p}}^{t_1}/\partial z) - (\partial w_{\mathbf{p}}^{t_1}/\partial x)$, obtained from cross differentiating (A.3) and (A.4) and with the chain rule enforced similarly, is

$$\begin{aligned}(s_y)_{\mathbf{p}}^{t_1} = {} & \alpha_1 \frac{\partial u_{\mathbf{p}}^{t_0}}{\partial z} - \frac{\partial w_{\mathbf{p}}^{t_0}}{\partial x} + \alpha_2 \frac{\partial v_{\mathbf{p}}^{t_0}}{\partial z} + \frac{g\Delta t}{2\rho_0}\left(\frac{\partial \rho_{\mathbf{p}}^{t_1}}{\partial x} + \frac{\partial \rho_{\mathbf{p}}^{t_0}}{\partial x}\right) - \frac{\alpha_3}{\rho_0}\left[\frac{\partial}{\partial z}\left(\frac{\partial P}{\partial x}\right)_{\mathbf{p}}^{t_1} + \frac{\partial}{\partial z}\left(\frac{\partial P}{\partial x}\right)_{\mathbf{p}}^{t_0}\right] \\ & + \frac{\Delta t}{2\rho_0}\left[\frac{\partial}{\partial x}\left(\frac{\partial P}{\partial z}\right)_{\mathbf{p}}^{t_1} + \frac{\partial}{\partial x}\left(\frac{\partial P}{\partial z}\right)_{\mathbf{p}}^{t_0}\right].\end{aligned} \tag{A.7}$$

For $f = 0$ used in the validation tests and $f \sim 10^{-4}\ \mathrm{s}^{-1}$ and $\Delta t \sim \mathrm{O}$ (5 min) or less used in the simulation of tidal internal waves, the parameter $\tilde{f} \ll 1$, and the coefficients in (A.6) and (A.7) are essentially the following: $\alpha_1 = 1$, $\alpha_2 = f\Delta t$, $\alpha_3 = \Delta t/2$, and $\alpha_4 = f\Delta t^2/4$, to better than 0.1% accuracy. Comparison of these coefficients shows that the pressure gradient terms in (A.6) are smaller than all the other terms by Δt. Keeping only the larger terms, the s_x equation is

$$(s_x)_{\mathbf{p}}^{t_1} = -\frac{\partial v_{\mathbf{p}}^{t_0}}{\partial z} + f\Delta t \frac{\partial u_{\mathbf{p}}^{t_0}}{\partial z}. \tag{A.8}$$

In (A.7), with $\alpha_3 = \Delta t/2$ the two pressure gradient terms at t_1 cancel out; but, the x and z derivatives for the two remaining pressure gradient terms at t_0 do not, because the x and z derivatives outside the parentheses are evaluated with respect to the (a, c) coordinates; that is, the chain rule applies. However, at the zeroth order, $(a, c) = (x, z)$, the two pressure gradient terms at t_0 do negate each other. Only at the next order, does a difference exist, since the relationship between (x, z) and (a, c) at higher order is

$$(a, c) = (x, z) - (u_{\mathbf{p}}^{t_0}, w_{\mathbf{p}}^{t_0})\Delta t + \mathrm{O}(\Delta t^2). \tag{A.9}$$

Therefore, the difference,

$$-\frac{\partial}{\partial z}\left(\frac{\partial P}{\partial x}\right)_{\mathbf{p}}^{t_0} + \frac{\partial}{\partial x}\left(\frac{\partial P}{\partial z}\right)_{\mathbf{p}}^{t_0},$$

between the two pressure gradient terms at t_0 is at most on the order of Δt. This means that the pressure gradient difference term is smaller than the other terms by Δt as the difference term is multiplied additionally by Δt in (A.7). Again retaining only the larger terms, (A.7) becomes

$$(s_y)_{\mathbf{p}}^{t_1} = \frac{\partial u_{\mathbf{p}}^{t_0}}{\partial z} - \frac{\partial w_{\mathbf{p}}^{t_0}}{\partial x} + f\Delta t \frac{\partial v_{\mathbf{p}}^{t_0}}{\partial z} + \frac{g\Delta t}{2\rho_0}\left(\frac{\partial \rho_{\mathbf{p}}^{t_1}}{\partial x} + \frac{\partial \rho_{\mathbf{p}}^{t_0}}{\partial x}\right). \tag{A.10}$$

The numerical time integration in this paper uses (A.8) and (A.10). These two equations can be shown readily using (A.9) to reduce to (14) in the limit of $\Delta t \to 0$.

Appendix B

In problems where high frequency surface gravity waves are of no interest and are to be excluded from the calculation, implicit time integration for the free surface height with large time steps can be adopted. The difficulty with the implicit time integration of the free surface height in a non-hydrostatic density-stratified system is that the subsurface velocity needed for the calculation cannot be determine a priori. With the semi-Lagrangian scheme, the following procedure mitigates the difficulty and obtains the free surface height implicitly.

The first step is to compute the particle displacement field. This step always generates noisy grid-scale distortion of the free surface when the time step is greater than the periods of high frequency surface grid-scale waves (noise). Nevertheless, this free surface distortion is not significant if at the start of the displacement calculation, the surface noise is minimal. The second step is to compute the particle's $\rho_{\mathbf{p}}^{t_1}$ from (20) and then $\mathbf{s}_{\mathbf{p}}^{t_1}$ from (A.8) and (A.10) and to estimate the particle's $w_{\mathbf{p}}^{t_1}$ by either using $w_{\mathbf{p}}^{t_1} = w_{\mathbf{p}}^{t_0} + (\mathrm{d}w_{\mathbf{p}}^{t_0}/\mathrm{d}t)\Delta t$ or some higher order schemes. At the same time, (21) can be rewritten as

$$\left(\mathbf{u}_{\mathbf{p}}\right)_{\eta}^{t_1} + \frac{g\Delta t}{2\rho_0}\left(\rho_{\mathbf{p}}\frac{\partial \eta_{\mathbf{p}}}{\partial x}\right)^{t_1} = \left(\mathbf{u}_{\mathbf{p}}\right)_{\eta}^{t_0} - \Delta t\mathbf{f} \times \left(\mathbf{u}_{\mathbf{p}}\right)_{\eta}^{t_0} - \frac{g\Delta t}{2\rho_0}\left(\rho_{\mathbf{p}}\frac{\partial \eta_{\mathbf{p}}}{\partial x}\right)^{t_0} + \Delta t F(\mathbf{u}_{\eta}) \tag{B.1}$$

with the entire right-hand side of (B.1) evaluated at t_0, where for simplicity the Coriolis term is now evaluated explicitly. Let $\mathbf{G}_{\mathbf{p}}^{t_1}$ denote the right-hand side of (B.1). The third step is to interpolate the calculated $\mathbf{s}_{\mathbf{p}}^{t_1}$, $w_{\mathbf{p}}^{t_1}$, and $\mathbf{G}_{\mathbf{p}}^{t_1} = (\mathbf{u}_{\mathbf{p}})_{\eta}^{t_1} + (g\Delta t/2\rho_0)(\rho_{\mathbf{p}}(\partial \eta_{\mathbf{p}}/\partial x))^{t_1}$ back to the fixed grid, $\mathbf{r} = (x, z)$ to obtain $\mathbf{s}_{\mathbf{r}}^{t_1}$, $w_{\mathbf{r}}^{t_1}$, and $\mathbf{G}_{\mathbf{r}}^{t_1}$ on the fixed grid (note the change of subscript). With these fixed grid variables now known, $\partial \mathbf{u}_{\mathbf{r}}^{t_1}/\partial z$ is determined from (5), and the velocity profile at t_1 is

$$\mathbf{u}_{\mathbf{r}}^{t_1}(z) = (\mathbf{u}_{\mathbf{r}})_{\eta}^{t_1} + \int_z \frac{\partial \mathbf{u}_{\mathbf{r}}^{t_1}}{\partial z}\,\mathrm{d}z. \tag{B.2}$$

Since $\mathbf{G}_{\mathbf{r}}^{t_1} = (\mathbf{u}_{\mathbf{r}})_{\eta}^{t_1} + (g\Delta t/2\rho_0)(\rho_{\mathbf{r}}(\partial \eta_{\mathbf{r}}/\partial x))^{t_1}$, (B.2) becomes

$$\mathbf{u}_{\mathbf{r}}^{t_1}(z) = \mathbf{G}_{\mathbf{r}}^{t_1} - \frac{g\Delta t}{2\rho_0}\left(\rho_{\mathbf{r}}\frac{\partial \eta_{\mathbf{r}}}{\partial x}\right)^{t_1} + \int_z \frac{\partial \mathbf{u}_{\mathbf{r}}^{t_1}}{\partial z}\,\mathrm{d}z. \tag{B.3}$$

The fourth step is to discretize (13) in time by the trapezoidal rule, i.e.,

$$\frac{\eta_{\mathbf{r}}^{t_1} - \eta_{\mathbf{r}}^{t_0}}{\Delta t} = -\frac{1}{2}\frac{\partial}{\partial x}\left[\left(\int_{-h}^{\eta} u(z)\,\mathrm{d}z\right)_{\mathbf{r}}^{t_1} + \left(\int_{-h}^{\eta} u(z)\,\mathrm{d}z\right)_{\mathbf{r}}^{t_0}\right]. \tag{B.4}$$

Using (B.3) for $\mathbf{u}_{\mathbf{r}}^{t_1}(z)$ and regrouping the terms, (B.4) becomes

$$\eta_{\mathbf{r}}^{t_1} - \frac{g\Delta t^2}{4\rho_0}\frac{\partial}{\partial x}\left(\int_{-h}^{\eta}\rho_\eta\frac{\partial\eta}{\partial x}\,\mathrm{d}z\right)_{\mathbf{r}}^{t_1} = \eta_{\mathbf{r}}^{t_0} - \frac{\Delta t}{2}\frac{\partial}{\partial x}\left[\left(\int_{-h}^{\eta}(\mathbf{G}+\Delta\mathbf{u})\,\mathrm{d}z\right)_{\mathbf{r}}^{t_1} + \left(\int_{-h}^{\eta}\mathbf{u}\,\mathrm{d}z\right)_{\mathbf{r}}^{t_0}\right], \tag{B.5}$$

which is a second order partial differential equation for the unknown $\eta_{\mathbf{r}}^{t_1}$. To be able to solve this equation practicably, η in the integration limit for t_1 will have to be assumed to be known approximately from the displacement calculation in step one given above. In this case, (B.5) is a linear second order partial differential equation,

$$\eta_{\mathbf{r}}^{t_1} - \frac{g\Delta t^2}{4\rho_0}\frac{\partial}{\partial x}\left[H_\eta\left(\rho_\eta\right)_{\mathbf{r}}^{t_1}\frac{\partial\eta_{\mathbf{r}}^{t_1}}{\partial x}\right] = \eta_{\mathbf{r}}^{t_0} - \frac{\Delta t}{2}\frac{\partial}{\partial x}\left[\left(\int_{-h}^{\eta}(\mathbf{G}+\Delta\mathbf{u})\,\mathrm{d}z\right)_{\mathbf{r}}^{t_1} + \left(\int_{-h}^{\eta}\mathbf{u}\,\mathrm{d}z\right)_{\mathbf{r}}^{t_0}\right], \tag{B.6}$$

solvable by conventional procedures.

Once $\eta_{\mathbf{r}}^{t_1}$ is determined, the remaining steps are to calculate $(\mathbf{u}_\eta)_{\mathbf{p}}^{t_1}$ using (21) and perform all the other operations described in Sections 3.2, 3.4 and 3.5 to formally determine w and u, as well as P, at $t = t_1$.

References

[1] G.P. Williams, Numerical integration of the three-dimensional Navier–Stokes equations for incompressible flow, J. Fluid Mech. 37 (1969) 727–750.

[2] A. Mahadevan, J. Oliger, R. Street, A nonhydrostatic mesoscale ocean model. Part I: well posedness and scaling, J. Phys. Oceanogr. 26 (1996) 1868–1880.

[3] J. Marshall, C. Hill, L. Perelman, A. Adcroft, Hydrostatic, quasi-hydrostatic, and nonhydrostatic ocean modeling, J. Geophys. Res. 102 (1997) 5733–5752.

[4] V. Casulli, A semi-implicit finite difference method for non-hydrostatic, free-surface flow, Int. J. Numer. Meth. Fluids 30 (1999) 425–440.

[5] K.B. Winters, H.E. Seim, T.D. Finnigan, Simulation of non-hydrostatic, density-stratified flow in irregular domains, Int. J. Numer. Meth. Fluids 32 (2000) 263–284.

[6] P.K. Smolarkiewicz, L.G. Margolin, A.A. Wyszogrodzki, A class of nonhydrostatic global models, J. Atmos. Sci. 49 (2001) 349–364.

[7] D.H. Peregrine, Long waves on a beach, J. Fluid Mech. 27 (1967) 815–827.

[8] J.M. Witting, A unified model for the evolution of nonlinear water waves, J. Comput. Phys. 56 (1984) 203–236.

[9] O. Nwogu, An alternative form of the Boussinesq equations for nearshore wave propagation, J. Waterway, Port, Coast. Ocean Eng. 119 (1993) 618–638.

[10] G.E. Wei, J.T. Kirby, S.T. Grilli, R. Subramanya, A fully nonlinear Boussinesq model for surface waves. Part 1. Highly nonlinear unsteady waves, J. Fluid Mech. 294 (1995) 71–92.

[11] C.Y. Shen, Constituent Boussinesq equations for waves and currents, J. Phys. Oceanogr. 31 (2001) 850–859.

[12] C.S. Yih, Stratified Fluids, Academic Press, New York, 1980 (Chapter 3).

[13] A. Staniforth, J. Côté, Semi-Lagrangian integration schemes for atmospheric models, Mon. Weather Rev. 119 (1991) 2206–2223.

[14] R.J. Purser, L.M. Leslie, An efficient semi-Lagrangian scheme using third-order semi-implicit time integration and forward trajectories, Mon. Weather Rev. 122 (1994) 745–756.

[15] T.J. Simons, Verification of numerical models of Lake Ontario. Part I. Circulation is spring and early summer, J. Phys. Oceanogr. 4 (1974) 507–523.

[16] A.F. Blumberg, G.L. Mellor, A description of a three-dimensional coastal ocean circulation model, in: N.S. Heaps (Ed.), Three-dimensional Coastal Ocean Circulation Models, Coastal and Estuarine Sciences, vol. 4, American Geophysical Union, Washington, DC, 1987, pp. 1–16.

[17] R.J. Purser, L.M. Leslie, An efficient interpolation procedure for high-order three-dimensional, semi-Lagrangian models, Mon. Weather Rev. 113 (1991) 2492–2498.

[18] B. Fornberg, Calculation of weights in finite difference formulas, SIAM Rev. 40 (1998) 685–691.

[19] J. Adams, Multigrid Software for Elliptic Partial Differential Equations: MUDPACK, NCAR Technical Note-357+STR, Feb. 1991, 51p.

[20] D.J. Brown, D.R. Christie, Fully nonlinear solitary waves in continuously stratified Boussinesq fluids, Phys. Fluids 10 (1998) 2569–2586.

[21] B. Turkington, A. Eydeland, S. Wang, A computational method for solitary internal waves in a continuously stratified fluid, Stud. Appl. Math. 85 (1991) 93–127.
[22] K.K. Tung, T.F. Chan, T. Kubota, Large amplitude internal waves of permanent form, Stud. Appl. Math. 66 (1982) 1–44.
[23] R.R. Long, Some aspects of the flow of stratified fluids. III. Continuous density gradients, Tellus 7 (1955) 342–357.
[24] J.R. Apel, J.R. Holbrook, A.K. Liu, J.J. Tsai, The Sulu Sea internal soliton experiment, J. Phys. Oceanogr. 15 (1985) 1625–1651.
[25] W. Alpers, Theory of radar imaging of internal waves, Nature 314 (1985) 245–247.
[26] J.R. Apel, M. Badiey, C.-S. Chiu, S. Finette, R. Headrick, J. Kemp, J.F. Lynch, A. Newhall, M.H. Orr, B.H. Pasewark, D. Tielbuerger, A. Turgut, K. von der Heydt, S. Wolf, An overview of the 1995 SWARM shallow-water internal wave acoustic scattering experiment, IEEE J. Oceanic Eng. 22 (1997) 465–500.
[27] L.A. Ostrovsky, Y.A. Stepanyants, Do internal solitons exist in the ocean?, Rev. Geophys. 27 (1989) 293–310.
[28] T. Matsuura, T. Hibiya, An experimental and numerical study of the internal wave generation by tide-topography interaction, J. Phys. Oceanogr. 20 (1990) 506–521.
[29] K.G. Lamb, Numerical experiments of internal wave generation by strong tidal flow across a finite amplitude bank edge, J. Geophys. Res. 99 (1994) 843–864.
[30] T. Gerkema, J.T.F. Zimmerman, Generation of nonlinear internal tides and solitary waves, J. Phys. Oceanogr. 25 (1995) 1081–1094.
[31] V. Vlasenko, Structure of large-amplitude internal solitary waves, J. Phys. Oceanogr. 30 (2000) 2172–2185.
[32] J. Small, J. Martin, The generation of non-linear internal waves in the Gulf of Oman, Cont. Shelf Res. 22 (2002) 1153–1182.